Ocean Engineering 266 (2022) 112872

Contents lists available at ScienceDirect

Ocean Engineering

journal homepage: www.elsevier.com/locate/oceaneng

Increased efficiency of hydrokinetic turbines through the use of an obstacle on the channel bottom

R. Espina-Valdés [a,*], V.M. Fernández-Álvarez [a], A. Gharib-Yosry [b], A. Fernández-Jiménez [a], E. Álvarez-Álvarez [a]

[a] GIFD Group, EP Mieres, University of Oviedo, Mieres, Spain
[b] Mechanical Power Department, Faculty of Engineering, Port Said University, Port-Said, Egypt

ARTICLE INFO

Keywords:
Hydrokinetic
Cross-flow
Obstacle
Rotor flow rate
Maximum-power-point

ABSTRACT

Nowadays, the growing demand for energy and the current shift towards the eradication of fossil fuels has led to continuous research into and development of alternative clean energies. Among these, one of the least investigated is the extraction of hydrokinetic energy in hydraulic channels. This article highlights an investigation focused on improving the performance of a hydrokinetic turbine installed in a hydraulic channel through the use of an obstacle on the channel bottom, thus providing a solution involving minimum investment and without the need for maintenance. It was found through a series of tests carried out in a hydrodynamic water tunnel that the power produced increases with the height of the obstacle. In addition, a validated numerical model facilitated the completion of the research by studying the influence of the height of the obstacle on the flow rate that passes through the turbine rotor. The latter representing the key factor in the generation of power together with the forces actuating on the blades. Under conditions analogous to those of the literature examples (with the turbine fully submerged), a power increase of about 25% was obtained in the tests.

1. Introduction

The renewable energy sector has not been spared from the effects of the COVID-19 (International Energy Agency, 2021). Pandemic and manufacturing processes, supply chains and investments have been affected, leading, once again, to a slowdown in the transition to a sustainable global energy model (Hosseini, 2020). Nevertheless, our responsibility as a society is to continue the path towards finding new, cleaner, and more sustainable sources of energy.

In addition to conventional renewable energies, there are other types of small-scale energy utilization that may be of great interest, such as systems for utilizing the energy present in river currents, artificial water channels or marine currents or tides. The energy that exists in flowing water currents is considered a low-carbon resource with an enormous power potential (Moran, Lopez, Moore, Müller, Hyndman). In fact, the International Energy Agency (IEA) has estimated a world energy potential of 120,000 TWh in the case of tidal currents (Caballero Santos, 2011) and more than 840 TWh in the case of low-velocity water currents of rivers and channels (IDAE, 2011). At present, the state of development of the use of the energy present in the currents is conducted by hydrokinetic turbines with know-how derived from the wind industry. The development of these devices is still in its embryonic stage, with demonstration applications to supply electrical energy in not connected to the electricity grid areas (Kumar and Sarkar, 2016). The power generated by a hydrokinetic turbines depend on the water velocity cubed, the area swept by blades, the water density and the efficiency of the conversion equipment (Mohammadi et al., 2020). The rated electrical power of the marine hydrokinetic turbines is generally much higher (>100 kW) than river and channel turbines (1–10 kW) (Roberts et al., 2016). Until now, the use of hydrokinetic turbines has been restricted mainly to water velocities higher than 1 m/s (Güney and Kaygusuz, 2010).

Hydrokinetic turbines can be classified according to the direction of flow and the position of the axis in two main groups: axial turbines with parallel axis and flow (similar to the designs of two-bladed and three-bladed horizontal axis wind turbines), and crossflow with perpendicular axis (horizontal or vertical in relation to the free surface) and flow, like the Savonius or Darrieus designs (Vermaak et al., 2014) (Patel et al., 2017a). In the existing developments to date, axial turbines present better conversion efficiency than crossflow ones, but these allow better use of the wet section. Additionally, vertical axis crossflow turbines

* Corresponding author.
E-mail address: espinarodolfo@uniovi.es (R. Espina-Valdés).

https://doi.org/10.1016/j.oceaneng.2022.112872
Received 18 March 2022; Received in revised form 13 September 2022; Accepted 8 October 2022
Available online 18 October 2022

Nomenclature

A_u	Turbine useful area, m^2
D	Turbine diameter, m
F_D	Drag forces, N
F_L	Lift forces, N
F_T	Thrust forces, N
g	Gravitational acceleration, m/s^2
h	Water height, m
H_r	Turbine hydraulic head, m
L	Blade length, m
n	Turbine rotational speed, rpm
p	Pressure, Pa
P_e	Electrical power, W
P_r	Hydraulic power, W
P_{rMPP}	Maximum hydraulic power, W
Q	Water flow rate, m^3/s
Q_r	Rotor flow rate, m^3/s
Q_{rMPP}	Flow rate in maximum power production, m^3/s
R_e	Reynolds number
v	Velocity, m/s
y	Upstream water depth, m
y_c	Critical depth, m
z	Obstacle height, cm

Greek symbols

η_e	Electrical efficiency
η_m	Mechanical efficiency
μ	Water viscosity, Kg/m·s
ρ	Water density, kg/m^3

Abbreviation

AFD	Adjustable frequency drive
AISI	American iron and steel institute
CFD	Computational fluid dynamics
HWT	Hydrodynamic water tunnel
MPP	Maximum power point
MPPT	Maximum power point continuously
O&M	Operation and maintenance
PMG	Permanent magnet generator
SCADA	Supervisory control and data acquisition
SIMPLE	Semi-implicit method for pressure-linked equations
SST	Shear stress transport
TURTLE	Turbine test laboratory equipment
URANS	Unsteady Reynolds-Average-Navier-Stokes
VOF	volume of fluid
3D	three-dimensional

allow electrical and electronic control equipment to be located out of the water, unlike axial turbines, whose equipment must be encapsulated when submerged. As analyzed by Patel et al. (2017b) through experimental investigations, the Darrieus turbine is one of the best options that can be used as a hydrokinetic turbine due to its high power coefficient. Therefore, the use of vertical axis cross-flow turbines reduces the initial investment, minimizes maintenance costs and increases the availability of the system (Hunt et al., 2020). The new technological challenge for the development of this type of turbines is the improvement of their efficiency even in operating conditions with very low speeds, for which

Table 1
Flow modifiers schemes.

a) (Salleh et al., 2020)

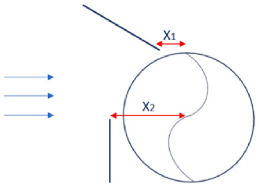

b) (Mosbahi et al., 2021)

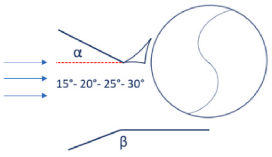

c) (Kang et al., 2021)

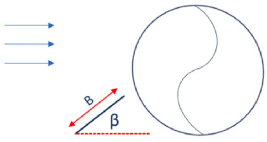

d) (Kailash et al., 2012)

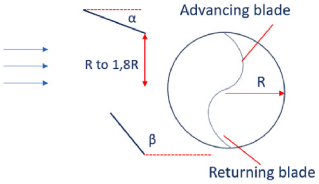

e) (Kaprawi et al., 2015)

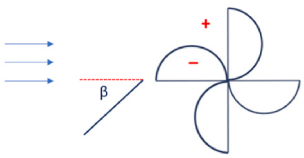

f) (Jeeva et al., 2021)

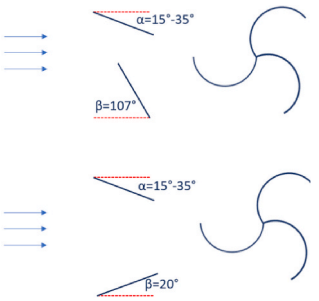

g) (Alizadeh et al., 2020)

h) (Sahim et al., 2014)

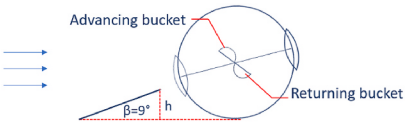

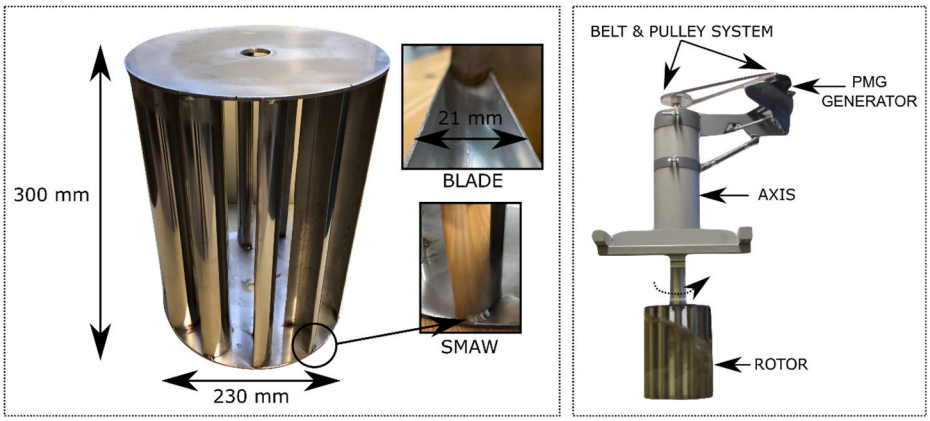

Fig. 1. Turbine design.

various methods have been studied.

Firstly, the development of a control algorithm which ensure that the maximum power of the turbine is continuously secured, named Maximum Power Point Tracking (MPPT) algorithm. For example, the research presented in (Alvarez et al., 2018) that proposes a simple solution based on a low cost power electronics control board running simple software. Additionally, the studies carried out by Jia et al. (2002) and Bundi et al. (2020) propose MPPT algorithms embedded in a low-cost electronic board for its application in turbines operating in high torque conditions.

Secondly, taking advantage of the variation of the current characteristics caused by the blockage generated by the turbine when the flow passes (Houlsby and Vogel, 2016). This results in three phenomena: an increase in the velocity of the fluid around the rotor, a change of the pressure in the wake, and the appearance of longitudinal pressure gradients due to the effects of the boundary layer (Glauert, 1933). Daskiran et al. (2016) investigated the blockage ratio effect on turbine performance and they found that the increment in blockage ratio from 0.03 to 0.98 enhanced its power coefficient from 0.437 to 2.254 and increased power generation from 0.56 kW to 2.86 kW. Kolekar et al. carried out experiments to understand the influence of free surface proximity on blockage effects and near-wake flow field, and therefore in the power obtained (Kolekar et al., 2019). Honnasiddaiah et al. (C M et al., 2021) analyzed the performance of a Savonius rotor for small-scale hydropower generation by modifying the bed slope, and they found power coefficient and torque coefficient improvements of up to 40% and 10%, respectively.

Thirdly, installing flow modifiers to increase the turbine performance, mainly in drag-based rotors. The simpler ones are vertical plates located upstream from the turbine. Different examples of studies in the research line of vertical plates with drag-based rotor turbines, are shown in Table 1 (elaborated by the authors) represented by horizontal two-dimensional models. The study of the influence of a double obstacle scheme in the performance of a turbine (Table 1–a) was done by Salleh et al. (2020) finding increments up to 30%. Mosbahi et al. (2021) analyzed the effect of an upstream deflector system (Table 1–b) in the performance of a twisted rotor by numerical simulations and experimental tests. Results showed that the proposed deflector improved its efficiency by 14%. Kang et al. (2021) described the effects of an upstream baffle on the flow characteristics and starting performance of a drag-type hydrokinetic rotor (Table 1–c). The results show that the negative torque is eliminated due to the introduction of the deflector.

Other experimental studies carried out showed that two deflectors placed in their optimal positions upstream of the flow increased the energy obtained (Kailash et al., 2012) (Table 1–d) and revealed that the angle of the deflector with regard to the current flow influences the performance of the turbine (Kaprawi et al., 2015) (Table 1–e) (Jeeva et al., 2021) (Table 1–f). For a Savonious model design, Alizadeh et al. (2020) investigated (using CFD model) the power generation improvement made by an upstream barrier (with at least the turbine height) that deviated the fluid flow from the reversing bucket (Table 1–g). The results of this analysis revealed that utilizing a barrier to its optimum length increases the maximum power generated by about 18%. Also, the experimental work carried out by Sahim et al. (2014) concluded that a single deflector plate placed upstream from a Darrieus-Savonious turbine increases the energy that it produces (Table 1–h).

Despite the increase in power production that the flow modifiers produce, their installation brings about a rise in solution costs and complicates the O&M tasks, i.e., causing the accumulation of residues and sediments (Martin-Short et al., 2015).

This research reveals an analysis and study of how an obstacle in the channel bottom, below the turbine, increases the power generated by a cross flow drag-based hydrokinetic turbine operating in high blockage conditions. The obstacle has a remarkably simple design which minimizes the cost of its installation, prevents any possible obstruction of the current flow, maintains the directions of the stream flow lines across the turbine, finally obtaining an increase in power in keeping with the height of the obstacle. The inclusion of the obstacle in the channel when designing a new project would not require specific maintenance. In the case of acting on existing channels, it would mean a slight modification in the structure of the channel, which would not require an increase in the maintenance cost of the original channel, since it is only a modification of the slopes of the bottom of the channel. If this solution of the obstacle at the bottom is compared with the use of deflectors, an elimination of the sediment problems can be seen in the low speed zones that affect the deflectors, where periodic maintenance work is necessary and takes up time of operation and raises costs.

In this work, two obstacle heights plus the no obstacle case have been studied to obtain sufficient information to achieve a consistent validation of the numerical model. Experimental studies with a larger number of obstacle heights studied can be found in the literature, such as the analyses of Patel et al. (Patel, Eldho, Prabhu).

In terms of blockage, the obstruction caused by the presence of the turbine rotor plays an important role. The flow characteristics are altered and therefore, the power results obtained will vary if the turbine is installed in another location with different dimensions than the test channel. Thus, if one wished to extrapolate these results to another installation, it would be necessary to apply a velocity correction method. Patel et al. introduced the methodology of correcting the velocity and efficiency of hydrokinetic turbines with a highly blocked channel geometry (Patel et al., 2019).

The study was carried out in the running water channel of the EPM of the University of Oviedo, and the results obtained have been used to validate a Computational Fluid Dynamics (CFD) numerical model. This numerical model was used to perform a parametric study with different obstacle heights and to analyze the causes of the increase in power

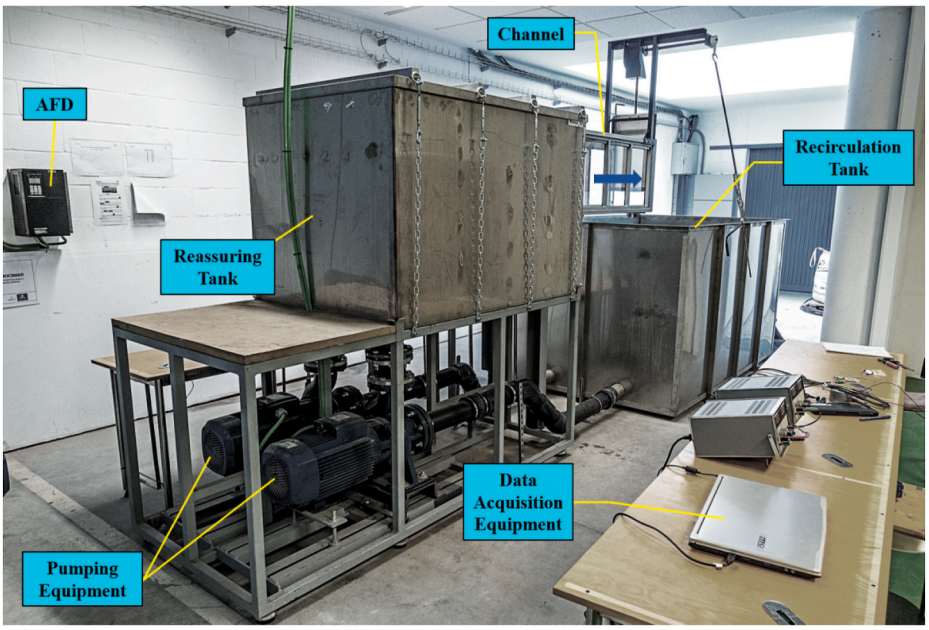

Fig. 2. Hydrodynamic water tunnel.

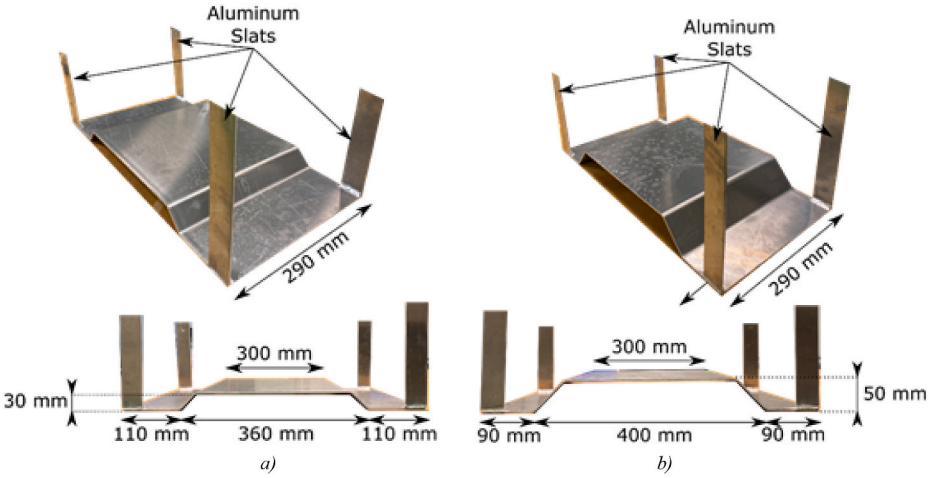

Fig. 3. Geometry of bed obstacles: a) 3 cm height and b) 5 cm height.

produced.

2. Laboratory materials

The elements used to carry out the tests were a turbine, a hydrodynamic water tunnel, two obstacles (same design and different heights) and a control system. The turbine rotor has 12 semi-circular blades 0.3 m high and 0.23 m wide, built with AISI 304 stainless steel to resist corrosion and dynamic forces, and shielded at the top and bottom to ensure adhesion even at fast rotational speeds. The blades have an angular separation of 30° with a semicircular section of 21 mm of diameter (Fig. 1). This type of turbine was selected because it has sufficient starting torque at low flow rates and has already been characterized in the laboratory and in the field.

The turbine is coupled to a vertical axis with radial and axial high standard waterproof bearings installed at a metallic bushing. This axis has in its upper part a belt and pulley system designed to multiplicate the rotational speed mechanically connected to a permanent magnet generator (PMG).

The experimental tests have been conducted in a hydrodynamic water tunnel (HWT) (Fig. 2) made up of tanks (reassuring and recirculation), hydraulic pumps, adjustable frequency drive (AFD), glass channel (0,5 m height, 0,3 m width and 1,5 length) and a monitoring-control system. The HWT can recirculate water flows up to 300 m^3/h.

The monitoring and control system, named TURbine Test Laboratory Equipment, TURTLE (designed by the researches of University of Oviedo Hydraulic Engineering Group) is made up of hardware components – two ultrasonic water height sensors (HC-SR04), two pump drives converters, electronic board to control the turbine operation, and PC– and a specially designed software which runs in the PC to perform the test and collect the data obtained (Álvarez-Álvarez et al., 2020).

The two obstacles (Fig. 3) have been made out of aluminium due to its low weight and firmness, designed to occupy all the channel width with heights of 3 cm and 5 cm.

3. CFD numerical model

To develop the numerical model, a complete three-dimensional geometry was generated incorporating the turbine, the reassuring tank, and the test channel (Fig. 4). The geometrical design has the real

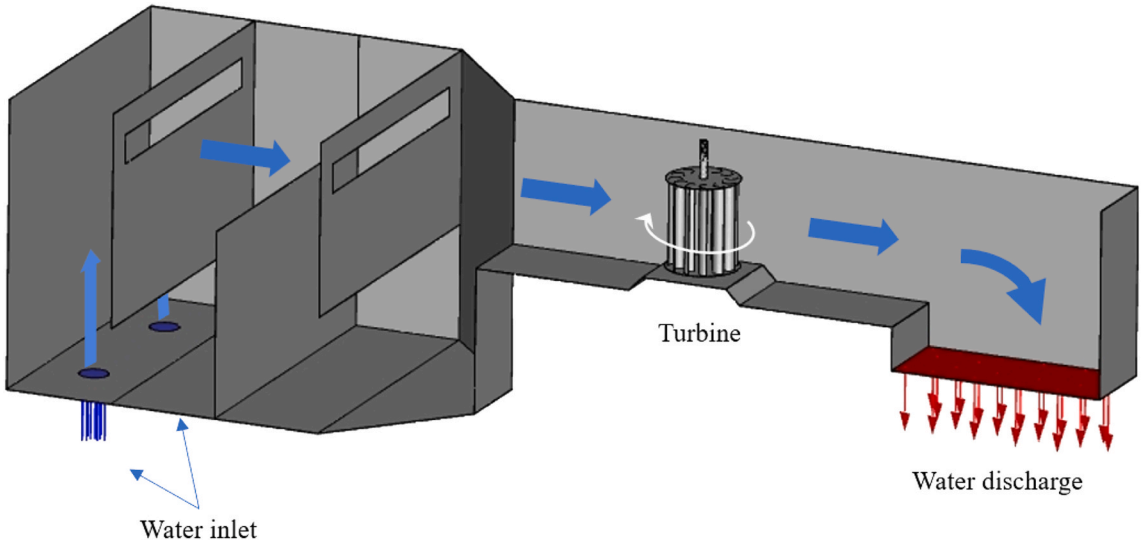

Fig. 4. HWT geometry.

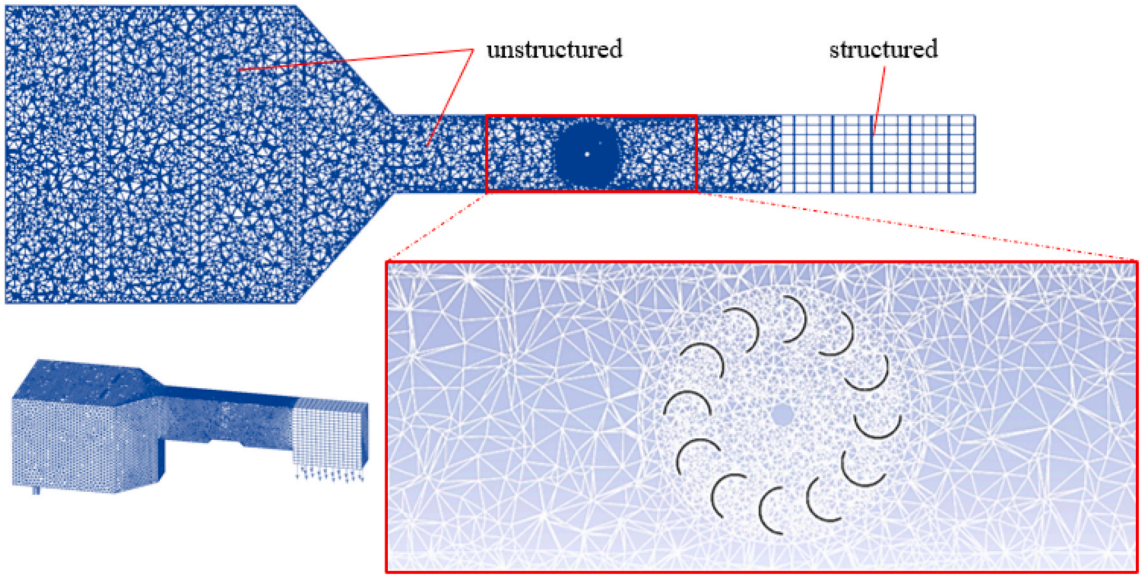

Fig. 5. Numerical model mesh.

dimensions of the hydrodynamic tunnel, including a rectangular prism-shaped area for the discharge of water from the channel (outlet) and two water inlet holes in the lower part of the reassuring tank. In addition, to guarantee the proper functioning of the model, the upper section of the domain was completely exposed to the air with a view to replicating the water flow free surface.

This same geometry was employed in the different simulations incorporating the different bed obstacles which were the object of the investigation. To obtain the numerical CFD model a cell mesh was built where the flow equations were solved (Fig. 5). For that purpose, the geometry was divided into 8 different volumes where an unstructured mesh based on tetrahedra (which has a good adaptation to complex geometries) was used, except for the water discharge area where a structured mesh based on rectangular prisms was employed due to its cubic shape. Incorporating the turbine in a cylindrical volume which rotates helped simulate the movement of the turbine with a good degree of accuracy as the unstructured mesh adapts perfectly to the turbine blades.

The number of cells of the mesh was set to 1,200,000 with satisfactory quality: 99.99% of the cells had a skewness value under 0.7. To study the dependence of the mesh with the power results and its influence on the computational time, five numbers of cells, 200,000, 500,000, 800,000, 1,200,000 and 1,500,000 were evaluated with the same flow rate and the range of rotational speeds that define the turbine power characteristics. With 1,200,000 cells a compromise between accuracy and computational time was reached.

The fluid volume model (VOF) has been selected to track the air-water free surface (Hirt and Nichols, 1981). The model solved the Unsteady Reynolds-Average-Navier-Stokes (URANS) for each cell of the entire domain (Riglin et al., 2015).

To obtain a turbine power characteristic from the no-load to the maximum load condition for a certain flow rate value, three steps were taken a) filling the canal with water (which was empty at the beginning) until the free surface stabilized; b) applying the condition of movement to the rotating mesh defined by introducing the inertial terms of the centrifugal forces and the Coriolis acceleration in the flow equations (Lanzafame et al., 2013); c) moving the rotating mesh with the different rotational speeds measuring the torque needed to maintain them

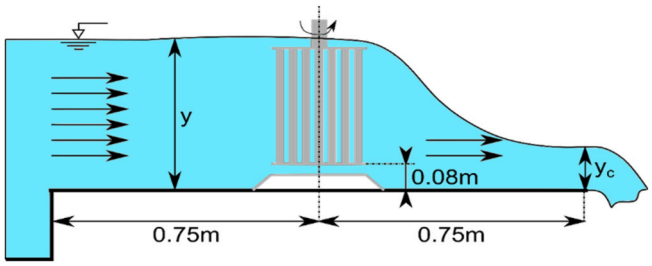

Fig. 6. Experimental test scheme.

constant. In the first two stages, convergence was achieved with 1000 iterations since they are stationary processes, while in the final phase, due to the mesh movement and its non-stationary condition, the convergence was achieved through a stabilization of the torque in 10 complete revolutions of the rotor. In this case, the value of the time step corresponding to a rotation of 3° was set, thereby varying it as a function of the rotational speed.

The boundary conditions applied were mass flow at the water inlets, pressure outlet at the discharge, and the upper part of the model (tank and channel) with normal atmospheric pressure (101.325 Pa). The surfaces of the tank, the channel and the turbine blades were defined as walls with no-slip condition. Water and air densities and viscosities were set to constant values (water:1.025 kg/m^3 and 1.003·10^{-3} kg/m·s; air: 1.225 kg/m^3 and 1.789·10^{-5} kg/m·s).

To resolve the URANS equations the solver Pressure-Implicit with splitting of Operators algorithm was used. Second order schemes were also applied for the discretization of the spatial and temporal derivatives in the equations. The semi-implicit method for pressure-linked equations (SIMPLE) was used in order to resolve the velocity-pressure coupling. The turbulence was simulated using the shear stress transport (SST) k-ω turbulence model, a combination of a k-ω model and a k-ε model suitable for complex flows (Bardina et al., 1997). This turbulence model is chosen since the average y+ is 0.93, and empowers accurate predictions of flow separation under adverse pressure gradients (Gorle et al., 2016). In addition, in the blade zone the meshing has cells within the boundary layer. To carry out the simulations of the numerical model, the ANSYS FLUENT V18.0 software was used (Ansys, 2018).

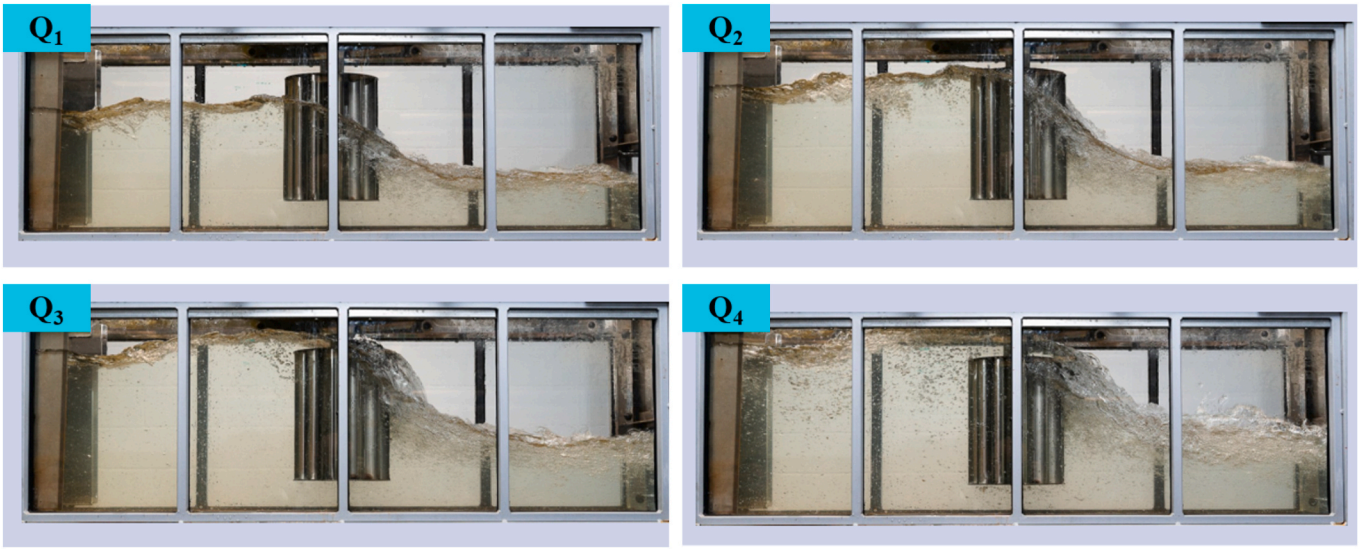

Fig. 7. Scenarios without bed obstacle.

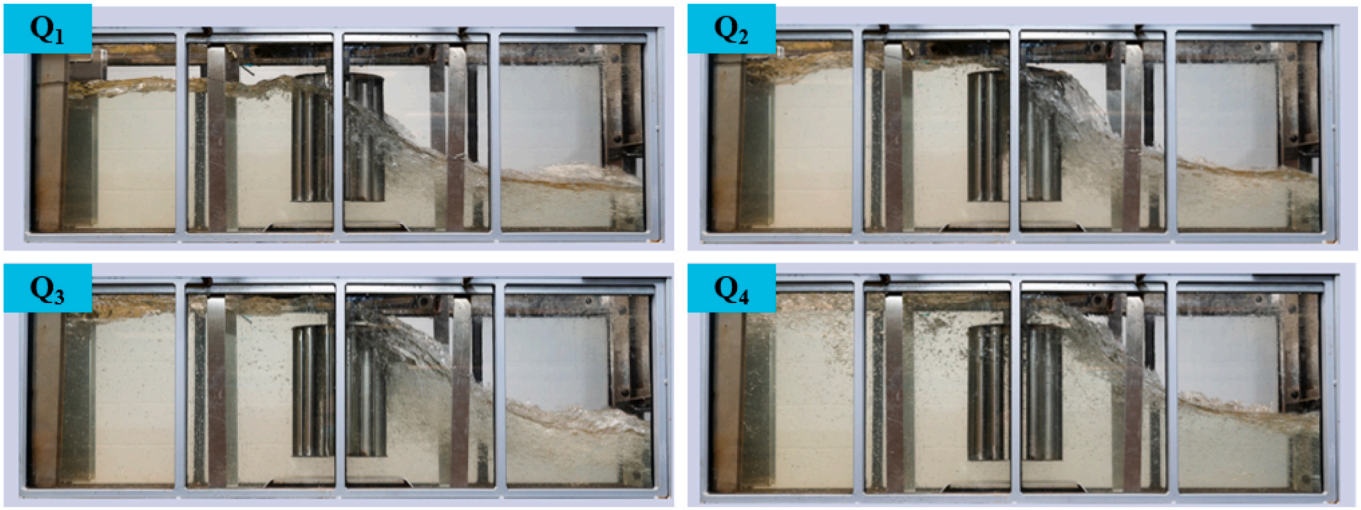

Fig. 8. Scenarios with 3 cm obstacle.

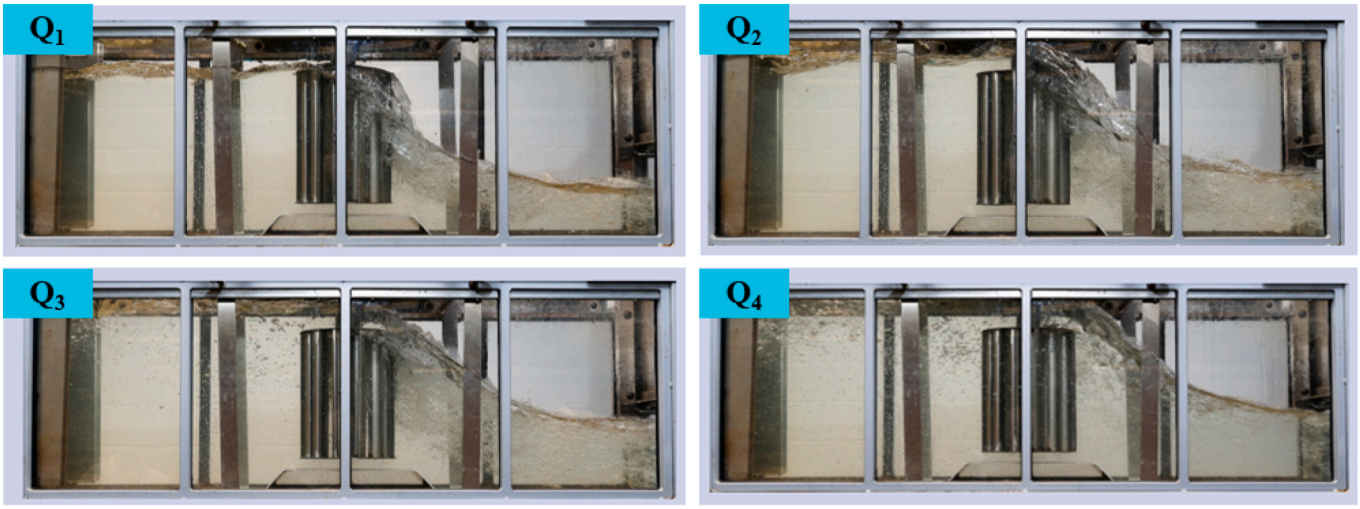

Fig. 9. Scenarios with 5 cm obstacle.

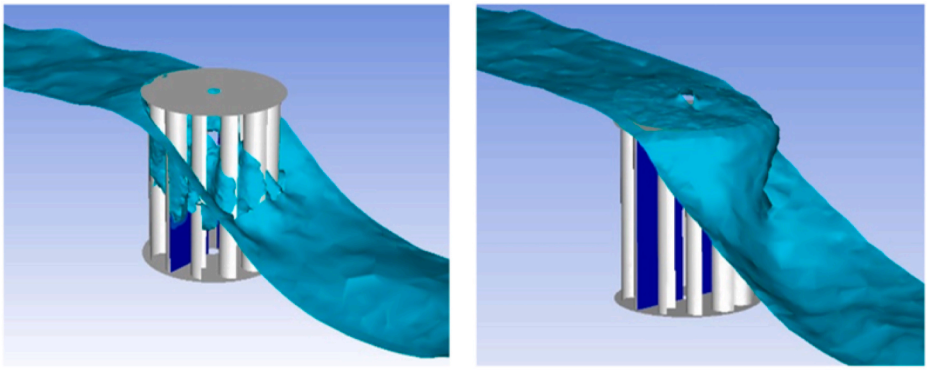

Fig. 10. Free surface and A_u for Q_3: a) no obstacle; b) 5 cm obstacle.

4. Experimental tests methodology

Three different set of tests were conducted: without bed obstacle, and with the 3 cm and the 5 cm height bed obstacles; each set with four flow rates: 0.055 m^3/s (Q_1), 0.064 m^3/s (Q_2), 0.072 m^3/s (Q_3) and 0.076 m^3/s (Q_4).

The position of the turbine and the obstacle in the tests are shown in Fig. 6, both elements upstream from the channel discharge at which critical flow conditions are reached. The channel slope is zero and the Reynolds number - $R_{ED} = \frac{\rho \bullet v \bullet D}{\mu}$ where ρ is water density, v is upstream water velocity, D is turbine diameter and μ is the water viscosity-in the experiment as a function of the diameter of the turbine is around $0.7*10^6$.

The different scenarios evaluated corresponding to the different flow rates and obstacles are shown in Figs. 7–9.

In scenarios Q_1 and Q_2 the presence of the obstacle increases the proportion of the turbine rotor that is submerged.

For all tests conducted the blockage ratio calculated as the wet transversal areas of turbine plus obstacle divided by that of the channel was kept within a range between 40% and 50%. The results are

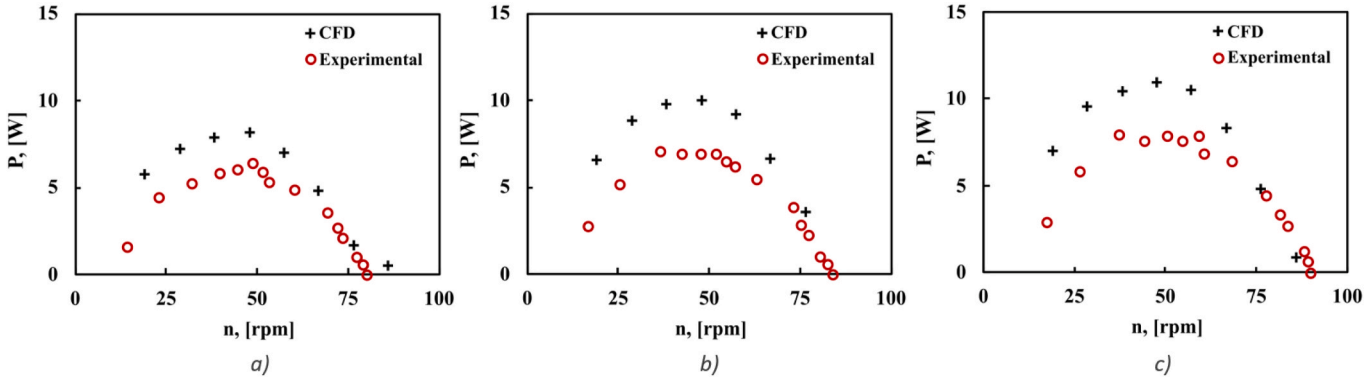

Fig. 11. Power characteristics experimental vs CFD for Q_4: a) no bed obstacle; b) 3 cm obstacle; c) 5 cm obstacle.

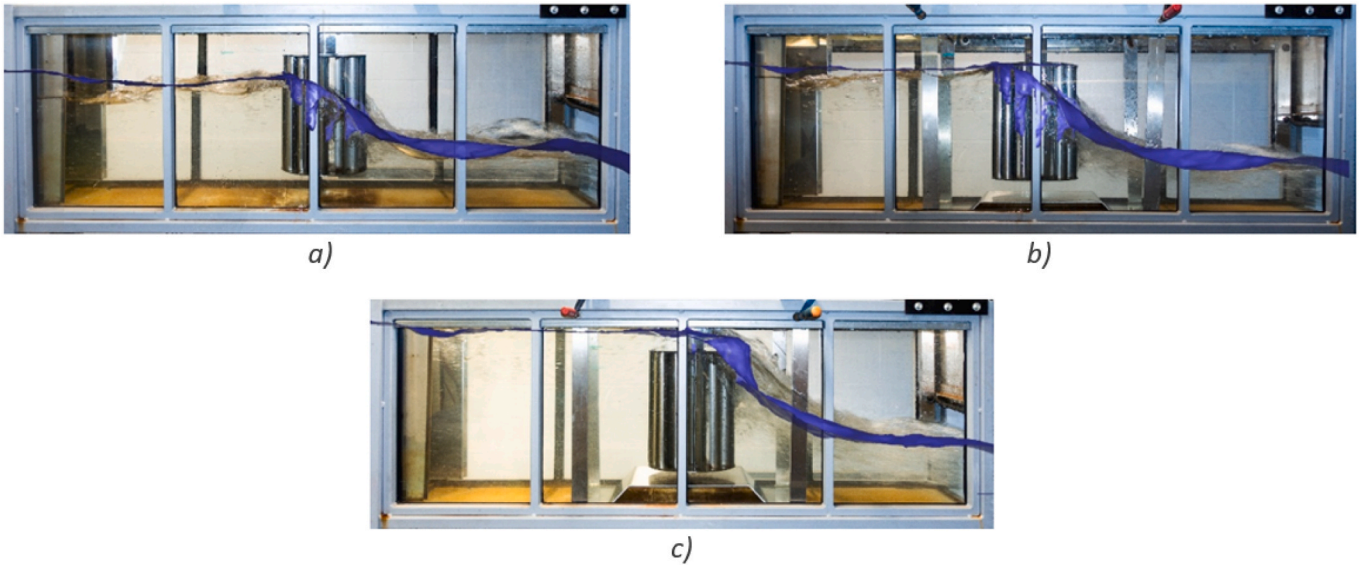

Fig. 12. Free surface experimental vs CFD results for Q_3: a) no obstacle; b) 3 cm obstacle; c) 5 cm obstacle.

conditioned by the size of the channel. The velocities and heights are the result of the size of the channel. Obviously, if this turbine configuration is tested in another scenario, the results will be different. To predict the real power of the turbine if it works in a river or canal with a large flow region, it would be necessary to take into account the velocity corrections widely studied in the literature, which are mainly due to the blockage effect.

5. Numerical model validation

The numerical model was validated with the experimental one by comparing their degree of similarity between results of power characteristics and free surfaces positions.

The power obtained with the CFD model consists of the rotor power (P_r) hereafter to be known as the hydraulic power:

$$P_r = \rho\, g\, H_r\, Q_r \tag{1}$$

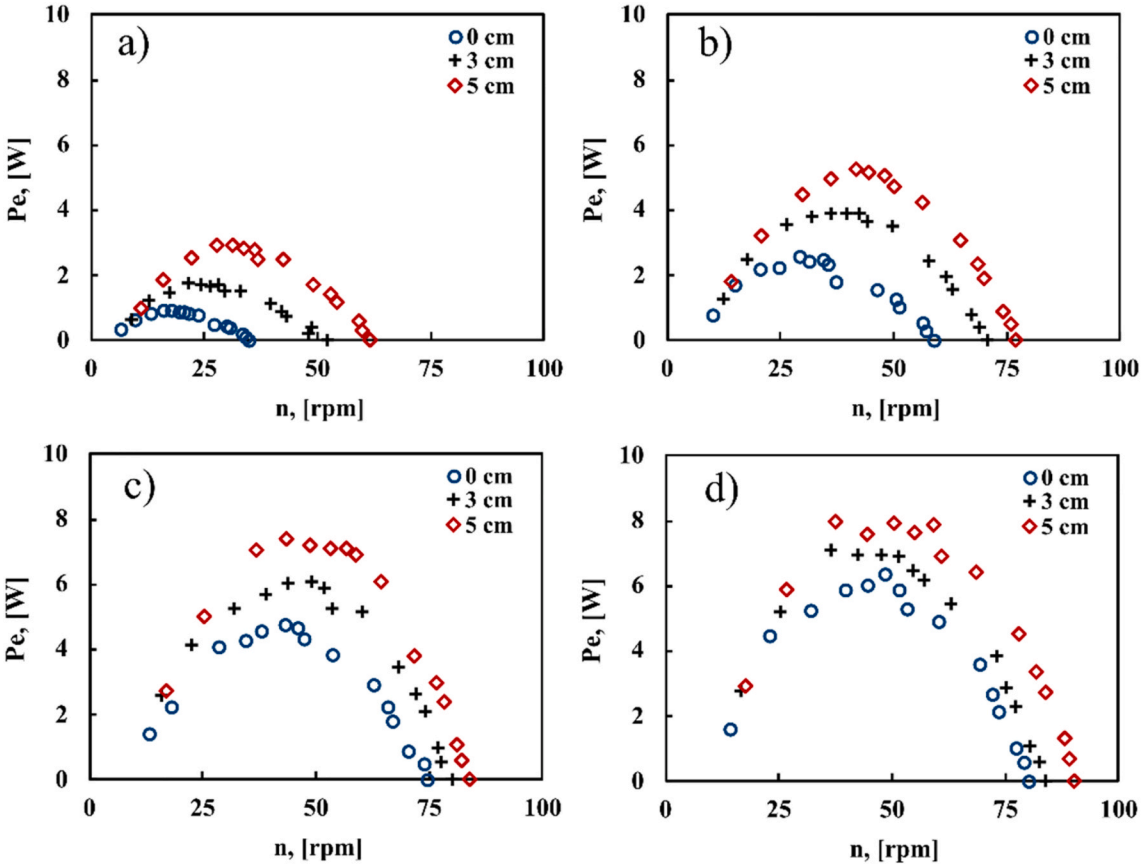

Fig. 13. Electrical power characteristics: a) Q_1; b) Q_2; c) Q_3; d) Q_4.

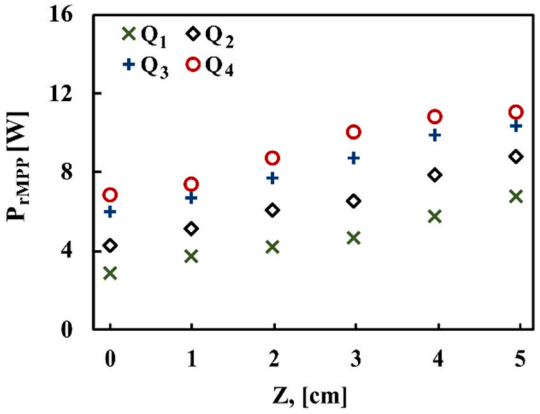

Fig. 14. Variation of P_{rMPP} with the obstacle height.

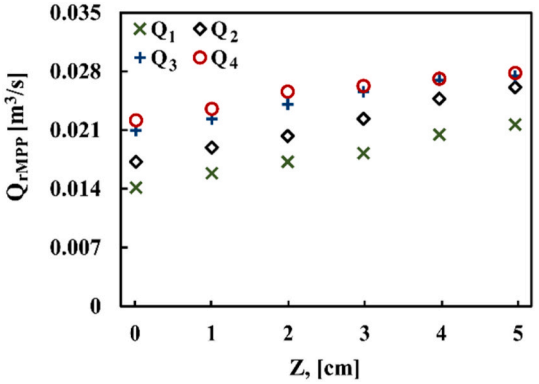

Fig. 15. Variation of Q_{rMPP} with the obstacle height.

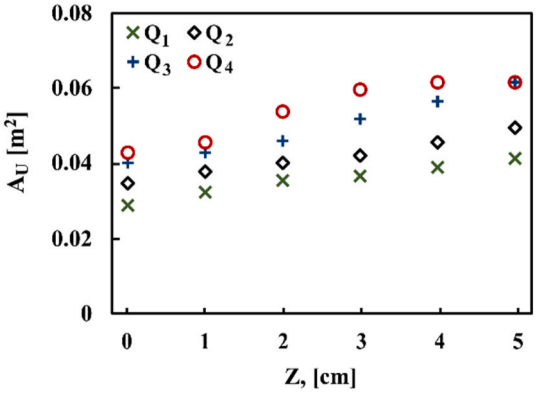

Fig. 16. Variation of A_u with the obstacle height.

where ρ is the density of the fluid, g is the gravity acceleration, H_r is the hydraulic head and Q_r is the rotor flow rate. The value of Q_r is determined by calculating the flow rate through the rotor-soaked area in a transversal-to-the-flow plane located in the middle of the turbine, named as useful area (A_u). Fig. 10 shows the free surface and A_u obtained for Q_3 with 3 and 5 cm obstacle heights.

However, the power obtained in the experimental tests corresponds to electrical power (P_e) that comprises the P_r and the mechanical and electrical performances of the installation, in accordance with the following expression:

$$P_e = \eta_e \, \eta_m \, P_r \tag{2}$$

where η_e is the electrical efficiency, η_m is the mechanical efficiency and P_r is the hydraulic power.

The results obtained for the different scenarios (example with Q_4 in Fig. 11) show that the power values obtained with the CFD model are significantly higher than the experimental ones. The differences increase as the rotational speed decreases from no load condition, where the maximum rotational speed is reached. The reason for that, is because the rotational speed reduction is induced to a progressive increment of the resistant torque implying higher mechanical losses in the pulley system (mechanical efficiency). The similarity between results provided full validation of the numerical model (see Fig. 12).

6. Results and discussion

Three types of tests have been conducted in the laboratory where the performance of the turbine has been studied in each of the planned scenarios. In the same way, these tests have been reproduced using validated CFD models. With the data obtained during the entire process, the behavior of the turbine and the power output were investigated and the consequences of introducing the obstacles were studied. In this section the results obtained in the experimental tests and in the simulations are shown and analyzed.

6.1. Electrical power characteristics

The tests to determine the characteristics of electrical power (P_e) plotted against rotational speed in experimental form (n) were performed from the no load (or no torque with maximum rotational speed) condition up to that of maximum torque (where the turbine stops) for the different flow rates. The results of the power features obtained show that the power values increase with the height of the obstacle for each value of rotational speed (Fig. 13). Also, for Q_1 and Q_2 (Fig. 13, a-b) the rotational speed range obtained for each feature is different as there is a considerable variation of the part not submerged with the obstacle height and the magnitude of the frictional power losses due to the pulley system. For each feature the point at which the turbine produces the maximum power known as MPP is of maximum interest as the turbine control systems will continuously ensure operability at those conditions (Alvarez et al., 2018).

6.2. Evolution of the maximum hydraulic power with the height of the obstacle

With the validated CFD model, it was possible to assess more cases by varying obstacle heights without performing physical tests in the laboratory channel. Thus, six cases have been simulated corresponding to obstacles from a height of 0 cm (without obstacle) to 5 cm in steps of 1 cm in height. Fig. 14 shows the evolution of the maximum hydraulic power (P_{rMPP}) versus the obstacle height always observing a linear dependence between variables with a nearly constant slope (around 0,5 W per 1 cm of obstacle height increment), for Q_1 and Q_2 scenarios. The same tendency is noted for Q_3 and Q_4 and obstacle heights up to 3 cm height, with a smooth increment of the maximum power for higher obstacles (4 and 5 cm).

6.3. Evolution of the rotor flow rate with the height of the obstacle

The same tendencies are observed with the Q_r in MPP (Q_{rMPP}) conditions and the height of the obstacle (Fig. 15): for Q_1 and Q_2 scenarios, the relationship between variables is linear with a constant slope, while for Q_3 and Q_4 the relationship is similar only for obstacle heights under 3 cm while for the greater ones, the increment of Q_{rMPP} with the obstacle height is lower.

For all cases, it was clear that the height of the obstacle implies a practically proportional rise of the upstream water free surface as a consequence of the high flow blockage conditions instigated by the

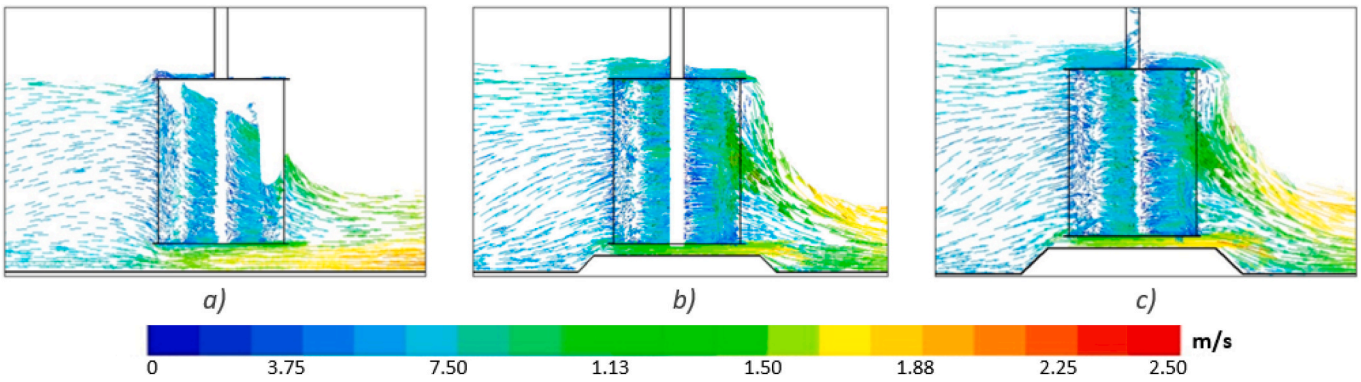

Fig. 17. Velocity vectors in the mid-transversal section for Q_3 and MPP conditions: a) no obstacle; b) 3 cm obstacle; c) 5 cm obstacle.

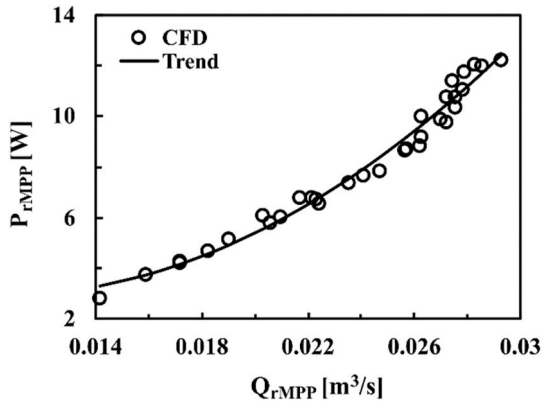

Fig. 18. Variation of P_{rMPP} with Q_{rMPP}.

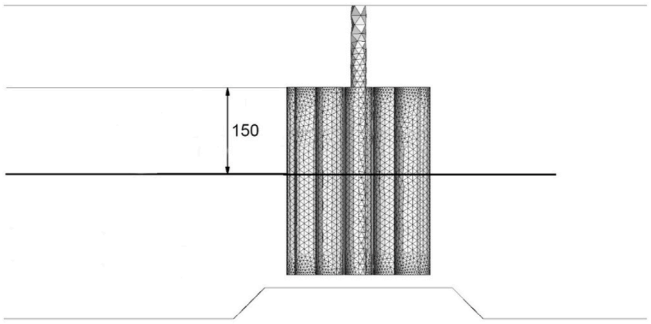

Fig. 19. Horizontal section location (mm).

turbine. The evolution of A_u with the height of the obstacle (Fig. 16) justifies the rotor flow rate trends observed for Q_1, Q_2, Q_3 and Q_4, with obstacle heights lower than 3 cm in the last two, as the height of the obstacle increases significantly the transversal area leading to a similar tendency in the rotor flow rate. While for the cases with A_u values close to the maximum one – Q_3 and Q_4 for obstacle heights higher that 3 cm – the influence of the obstacle height in the rotor flow rate is only produced by the increment of the water velocity through the turbine due to the proximity of the critical point of discharge, that makes that the rise of the elevation of the water surface is lower that height of the obstacle; as an example, Fig. 17 shows the water velocity vectors in the mid-transversal section of the turbine.

6.4. Evolution of maximum hydraulic power and rotor flow rate

Fig. 18 represents the relationship between the P_{rMPP} and Q_{rMPP} for all cases simulated in this study. This curve shows a slightly quadratic relationship between both variables which indicates that increments in the power production by the height of the obstacle are brought about by two factors: the rotor flow rate itself and the turbine head always bearing in mind that the upstream height increases with the height of the obstacle while the downstream critical height is kept constant for each water flow rate.

6.5. Forces actuating on the turbine blades

From the results of the CFD simulations, it was possible to study the fields of relative water velocities and pressure for the different flow rates at each MPP conditions, thereby determining the effects of the height of the obstacle in the forces actuating on the blades. These fields have been analyzed in a horizontal section located at 150 mm from the upper turbine section (Fig. 19), which is considered representative of the submerged sections.

Initially it can be detected that the values of the pressure around the blades increase in magnitude with the height of the obstacle, see for example the case of Q_3 (Fig. 20), where the white color represents air.

The increase in pressure is derived from the variation in the height of the water free surface upstream when the obstacle is placed, which induces a greater speed through the turbine (the variation of the free surface height is less in the turbine than upstream). This phenomenon was analyzed by Patel et al. (2018) and is based on the concept of increased stagnation pressure in the turbine blades and impulse momentum principle.

The study of the pressure and relative velocity fields also determine the forces present in the turbine blades. In order to carry out an analysis of the forces and in the absence of aerodynamic profiles of the blades, the study is conducted on the convex and concave faces of each blade, defining different forces: drag forces (F_D) in areas of both low pressure and relative water velocities (appear in the blades due to the wake generated by the rotational movement; thrust forces (F_T), in high pressure zones due to the flow stagnation (no water velocity); and lift forces (F_L), in zones of low pressure and high flow velocity in a direction parallel to the blade. As a representative example, Fig. 21 shows the pressure and relative velocity fields for the scenario of Q_3, 3 cm height obstacle, and MPP conditions, as well as the forces on the blades aligned to the flow direction (1 and 7), and those offering resistance (4 and 10). Note that these blades have been chosen because they represent the extreme conditions, while the rest of the blades are set to more intermediate ones.

F_T and F_D forces are present on blades 4 and 10. In blade 4 the F_T force acts on the concave face while F_D on the convex one, both generate torque in the direction of the turbine rotation (positive torque), while in blade 10, F_T and F_D are on the convex and concave faces respectively generating torque resisting the rotational movement (negative torque). In the case of blades 1 and 7, the F_T and F_L forces appeared on the convex

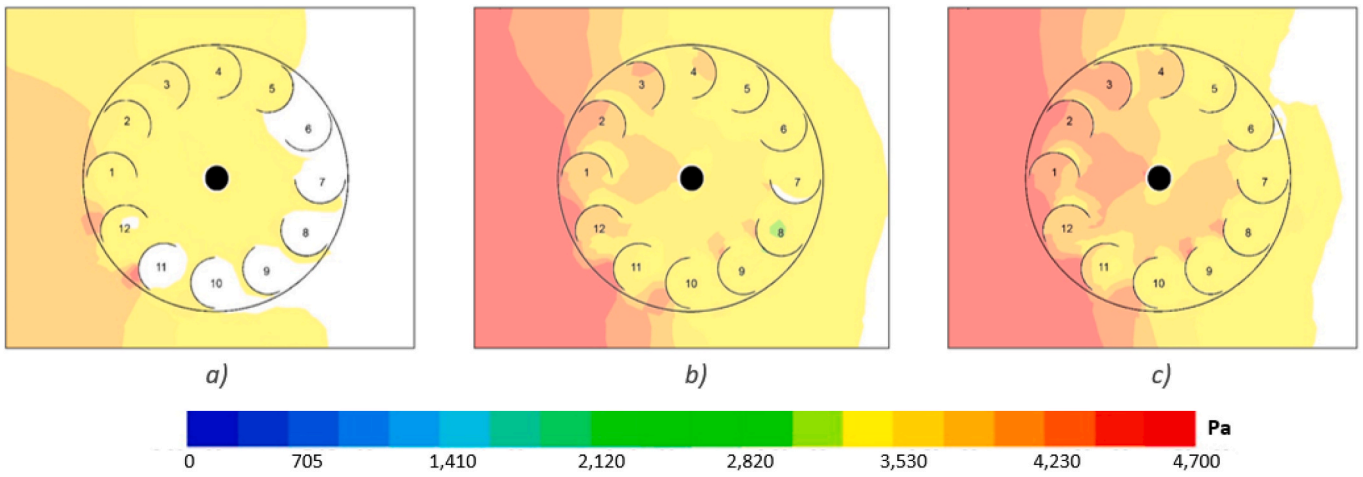

Fig. 20. Pressure field for Q_3 and MPP conditions: a) no obstacle; b) 3 cm obstacle; c) 5 cm obstacle.

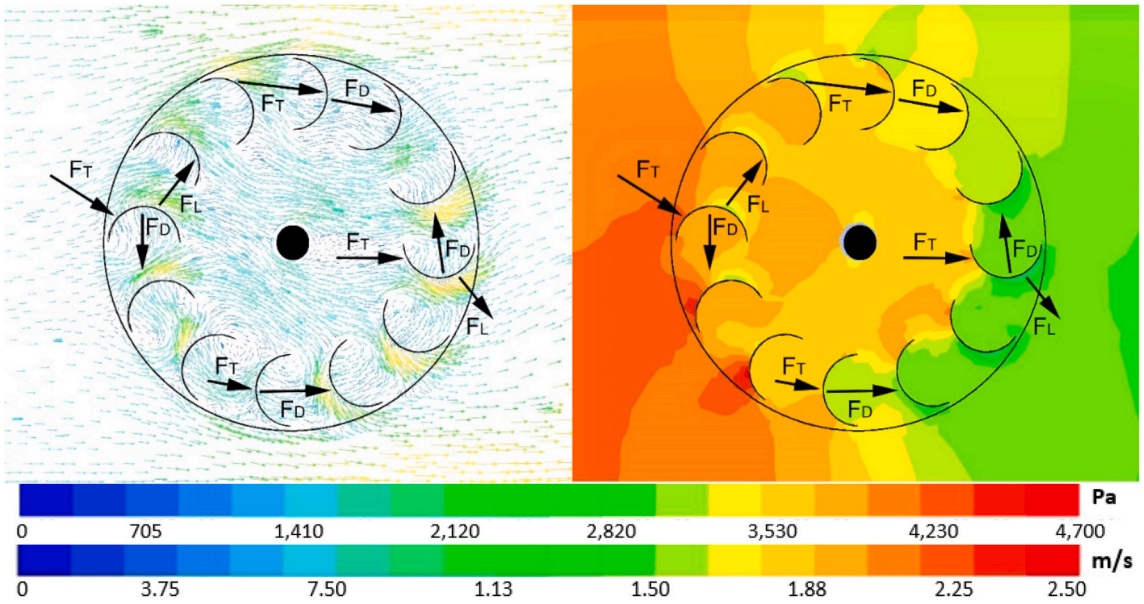

Fig. 21. Forces, relative velocity, and pressure fields (Q_3, 3 cm obstacle and MPP).

faces generating positive torque, while F_D forces appear on the concave ones creating negative torque. Figs. 22 and 23 show the pressure distribution along blades 1–7, and 4–10 respectively, with important variations in the cases in which F_T and F_L appear on the same face.

With the pressure distribution along the faces of the blade considered as positive pressure when it creates positive torque and negative in the opposite case, Figs. 24 and 25 represent the net pressure along blades 1–7 and 4–10 for Q_3 at MPP conditions with no obstacle, 3 cm and 5 cm height obstacle. In general, it can be the observed that the higher the height of the obstacle the greater the pressure values on the blades which in turn increases the torque in the sense of rotation. Additionally, it can be seen in Fig. 24, that on blades 1 and 7 the distribution of net pressure, half with negative values and half with positive values all along the blades result in a very low force and therefore torque. Therefore blades 1 and 7 have little influence on the turbine rotation and the obstacle presence does not produce any effect. However, blades 4 and 10 (Fig. 25) are crucial in order to generate movement and are significantly affected by the height of the obstacle.

7. Conclusions

The research provides an analysis of the increment in the power production of a drag-based water hydrokinetic turbine obtained by using a simple design of an obstacle on the bottom of the channel where the turbine is installed. Also, the turbine was located upstream at a critical discharge point and due to its dimensions prompted a high flow blockage (around 50%) The simplicity of the inclusion of this obstacle and the lack of O&M present this alternative as something which may feasibly be included in new industrial scale installations.

In a set of laboratory tests and by using a validated CFD model it was found that the power produced by the turbine increases with the height of the obstacle. The numerical model provided sufficient evidence to suggest that the water flow rate through the turbine rotor was the key factor which attributed to this increment in power production as it is largely dependent on the height of the obstacle, with the same tendencies observed with the power generation. For a fixed flow rate, the height of the obstacle entails an elevation of the water free surface upstream from the turbine which leads to an increment of rotor flow by increasing the wetted turbine transversal area up to its maximum, and when it is reached, for higher obstacles, increasing the water velocity

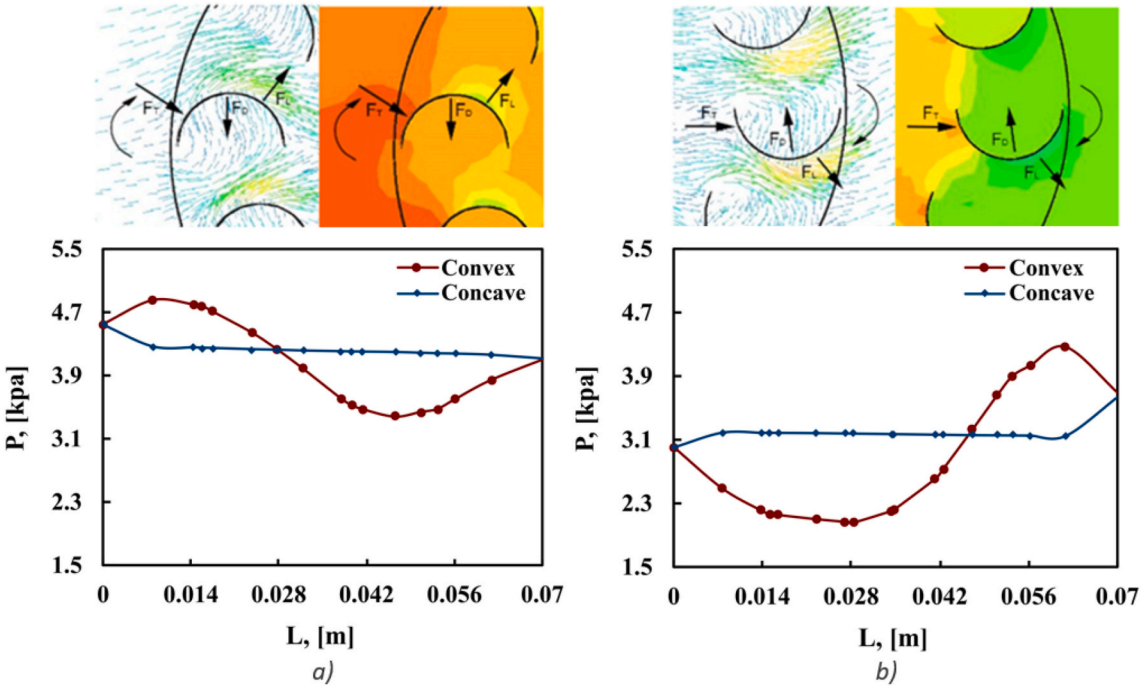

Fig. 22. Pressure distributions along (a) blade 1 and (b)blade 7 (Q_3, 3 cm obstacle and MPP).

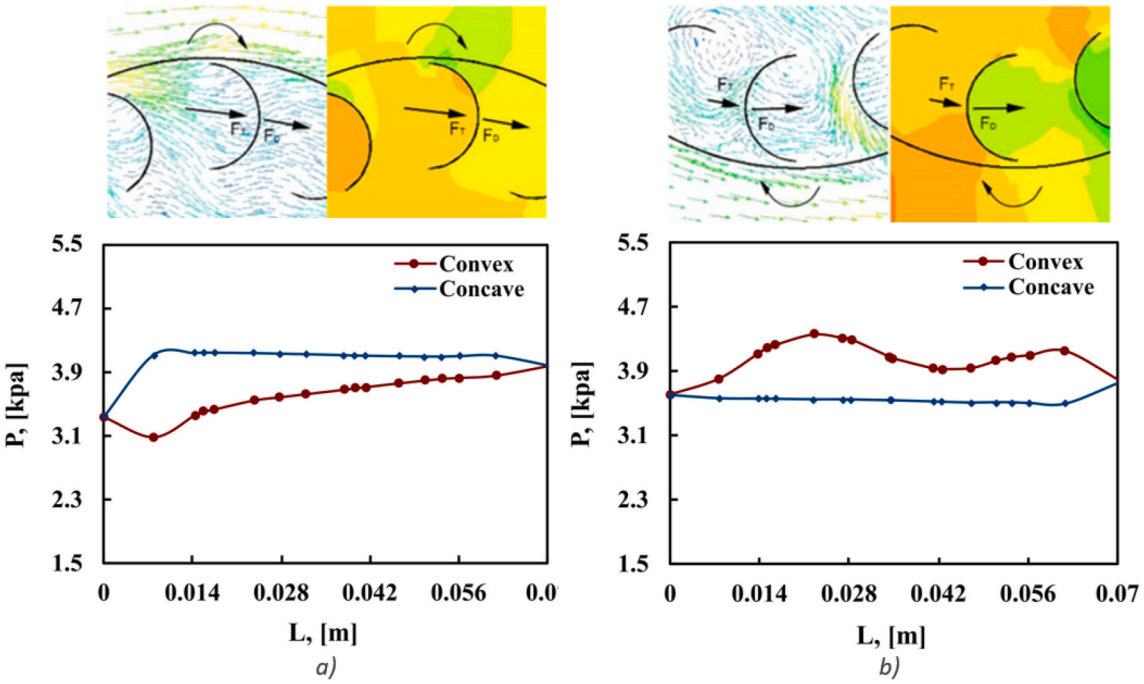

Fig. 23. Pressure distributions along (a) blade 4 and (b) blade 10 (Q_3, 3 cm obstacle and MPP).

due to the effect of the downstream critical point, as the water elevation is lower than the height of the obstacle.

The rise in the flow rate also occasions the same effect in the turbine hydraulic head, due to the high blockage conditions of installation, resulting both in a multiplication of the power production. Under conditions analogous to those of the literature examples (with the turbine fully submerged), a power increase of about 25% was obtained in the tests.

In addition, from the tests conducted the forces on the rotor blades have been studied from the pressure and velocity fields obtained in the numerical model. The effect of the height of the obstacles in the forces was identified and highlighted the fact that the obstacle height increased the net pressure, and therefore the torque produced on the blades, as they are placed transversally to the flow.

CRediT authorship contribution statement

R. Espina-Valdés: Investigation, Methodology, Validation, Formal analysis, Writing – original draft. **V.M. Fernández-Álvarez:** Investigation, Methodology, Data curation, Validation, Formal analysis. **A.**

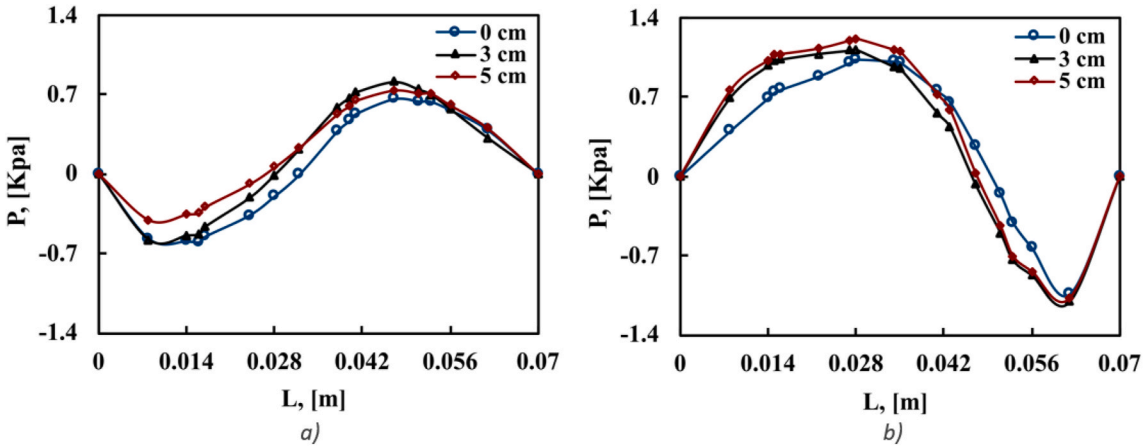

Fig. 24. Net pressure along (a) blade 1 and (b) blade 7 (Q_3 and MPP).

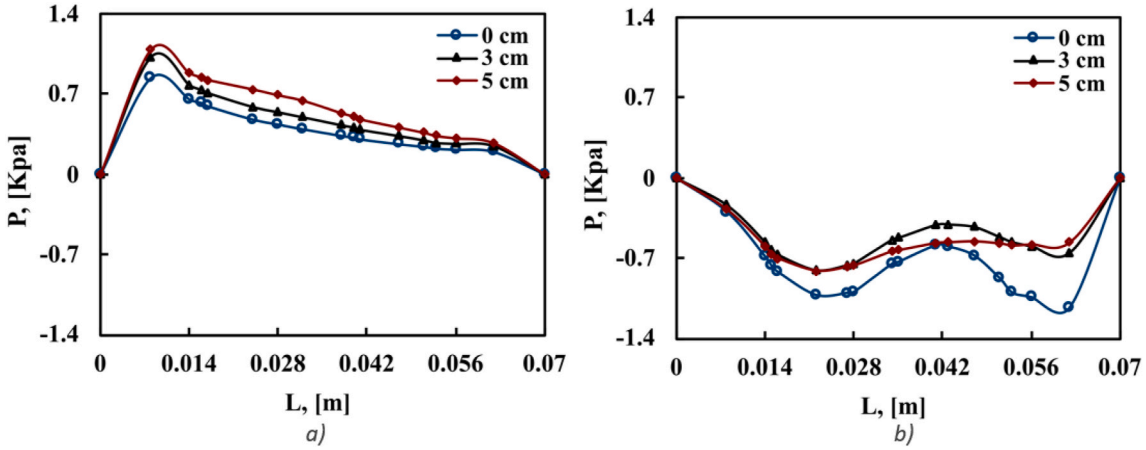

Fig. 25. Net pressure along (a) blade 4 and (b) blade 10 (Q_3 and MPP).

Gharib-Yosry: Investigation, Methodology, Formal analysis. **A. Fernández-Jiménez:** Investigation, Methodology, Data curation, Validation, Formal analysis. **E. Álvarez-Álvarez:** Conceptualization, Ideas, Writing – original draft, Writing – review & editing, Formal analysis, Supervision.

Declaration of competing interest

The authors declare that they have no known competing financial interests or personal relationships that could have appeared to influence the work reported in this paper.

Data availability

Data will be made available on request.

References

Alizadeh, H., Jahangir, M.H., Ghasempour, R., 2020. CFD-based improvement of Savonius type hydrokinetic turbine using optimized barrier at the low-speed flows. Ocean. Eng. 202 (March), 107178.

Alvarez Alvarez, E., Rico-Secades, M., Corominas, E.L., Huerta-Medina, N., Soler Guitart, J., 2018. Design and control strategies for a modular hydroKinetic smart grid. Int. J. Electr. Power Energy Syst. 95, 137–145.

Álvarez-Álvarez, E., Rico-Secades, M., Fernández-Jiménez, A., Espina-Valdés, R., Corominas, E.L., Calleja-Rodríguez, A.J., 2020. Hydrodynamic water tunnel for characterization of hydrokinetic microturbines designs. Clean Technol. Environ. Policy 22 (9), 1843–1854.

Ansys, 2018. ANSYS Fluent User's Guide, 18.1. Canonsburg, PA.

Bardina, J.E., Huang, P.G., Coakley, T.J., 1997. Turbulence modeling validation, testing, and development. NASA Tech. Memo. 110446, 8–20.

Bundi, J.M., Ban, X., Wekesa, D.W., Sun, Y., 2020. Advanced gain-scheduled control of A DFIG based on a H-Darrieus wind turbine for maximum power tracking and frequency support. Control Eng. Appl. Informat. 22 (2), 23–32.

C M, S., Honnasiddaiah, R., Hindasageri, V., Madav, V., 2021. Studies on application of vertical axis hydro turbine for sustainable power generation in irrigation channels with different bed slopes. Renew. Energy 163, 845–857.

Caballero Santos, C., 2011. Estudio de plantas de producción de energías renovables con aprovechamiento de la energía del mar. Universidad Carlos III de Madrid, Leganés.

Daskiran, C., Riglin, J., Oztekin, A., 2016. Numerical analysis of blockage ratio effect on a portable hydrokinetic turbine. In: Fluids Engineering, vol. 7. V007T09A064.

Glauert, H., 1933. Wind tunnel interference on wings, bodies and airscrews. Aeronaut. Res. Comm. 1566, 1–52.

Gorle, J.M.R., Chatellier, L., Pons, F., Ba, M., 2016. Flow and performance analysis of H-Darrieus hydroturbine in a confined flow: a computational and experimental study. J. Fluid Struct. 66, 382–402.

Güney, M.S., Kaygusuz, K., 2010. Hydrokinetic energy conversion systems: a technology status review. Renew. Sustain. Energy Rev. 14 (9), 2996–3004. Elsevier Ltd.

Hirt, C., Nichols, B., 1981. Volume of fluid (VOF) method for the dynamics of free boundaries. J. Comput. Phys. 39 (1), 201–225.

Hosseini, S.E., 2020. An outlook on the global development of renewable and sustainable energy at the time of COVID-19. Energy Res. Social Sci. 68 (April), 101633.

Houlsby, G.T., Vogel, C.R., 2016. The power available to tidal turbines in an open channel flow. Proc. Inst. Civ. Eng. - Energy 170 (1), 12–21.

Hunt, A., Stringer, C., Polagye, B., 2020. Effect of aspect ratio on cross-flow turbine performance. J. Renew. Sustain. Energy 12 (5).

IDAE, 2011. Plan de Energías Renovables 2011- 2020.

International Energy Agency, 2021. Global energy review 2021. Glob. Energy Rev. 2020, 1–36.

Jeeva, B., Sandeep, S.J., Ramsundram, N., Prasanth, M., Praveen, B., 2021. Experimental investigation of three bladed inclined savonius hydrokinetic turbine by using deflector plate. IOP Conf. Ser. Mater. Sci. Eng. 1146 (1), 012009.

Jia, Y., Yang, Z., Cao, B., 2002. A new maximum power point tracking control scheme for wind generation. In: PowerCon 2002 - 2002 International Conference on Power System Technology, Proceedings, vol. 1, pp. 144–148.

Kailash, G., Eldho, T.I., Prabhu, S.V., 2012. Performance study of modified savonius water turbine with two deflector plates. Int. J. Rotating Mach. 2012.
Kang, C., Zhao, H., Zhang, Y., Ding, K., 2021. Effects of upstream deflector on flow characteristics and startup performance of a drag-type hydrokinetic rotor. Renew. Energy 172, 290–303.
Kaprawi, S., Santoso, D., Sipahutar, R., 2015. Performance of combined water turbine darrieus- savonius with two stage savonius buckets and single deflector. Int. J. Renew. Energy Resour. 5, 217–221.
Kolekar, N., Vinod, A., Banerjee, A., 2019. On blockage effects for a tidal turbine in free surface proximity. Energies 12 (17), 3325.
Kumar, D., Sarkar, S., 2016. A review on the technology, performance, design optimization, reliability, techno-economics and environmental impacts of hydrokinetic energy conversion systems. Renew. Sustain. Energy Rev. 58, 796–813.
Lanzafame, R., Mauro, S., Messina, M., 2013. Wind turbine CFD modeling using a correlation-based transitional model. Renew. Energy 52, 31–39.
Martin-Short, R., Hill, J., Kramer, S.C., Avdis, A., Allison, P.A., Piggott, M.D., 2015. Tidal resource extraction in the Pentland Firth, UK: potential impacts on flow regime and sediment transport in the Inner Sound of Stroma. Renew. Energy 76, 596–607.
Mohammadi, S., Hassanalian, M., Arionfard, H., Bakhtiyarov, S., 2020. Optimal design of hydrokinetic turbine for low-speed water flow in Golden Gate Strait. Renew. Energy 150, 147–155.
Moran, E.F., Lopez, M.C., Moore, N., Müller, N., Hyndman, D.W., 2018. Sustainable hydropower in the 21st century. Proc. Natl. Acad. Sci. USA 115 (47), 11891–11898.
Mosbahi, M., et al., 2021. Performance improvement of a drag hydrokinetic turbine. Water 13 (3), 273.
Patel, V., Eldho, T.I., Prabhu, S.V., 2019. Velocity and performance correction methodology for hydrokinetic turbines experimented with different geometry of the channel. Renew. Energy 131, 1300–1317.
Patel, V., Bhat, G., Eldho, T.I., Prabhu, S.V., 2017a. Influence of overlap ratio and aspect ratio on the performance of Savonius hydrokinetic turbine. Int. J. Energy Res. 41 (6), 829–844.
Patel, V., Eldho, T.I., Prabhu, S.V., 2017b. Experimental Investigations on Darrieus Straight Blade Turbine for Tidal Current Application and Parametric Optimization for Hydro Farm Arrangement, vol. 17. Elsevier Ltd.
Patel, V., Eldho, T.I., Prabhu, S.V., 2018. Theoretical study on the prediction of the hydrodynamic performance of a Savonius turbine based on stagnation pressure and impulse momentum principle. Energy Convers. Manag. 168, 545–563.
Patel, V., Eldho, T.I., Prabhu, S.V., 2019. Performance enhancement of a Darrieus hydrokinetic turbine with the blocking of a specific flow region for optimum use of hydropower. Renew. Energy 135, 1144–1156.
Riglin, J., Chris Schleicher, W., Liu, I.-H., Oztekin, A., 2015. Characterization of a micro-hydrokinetic turbine in close proximity to the free surface. Ocean. Eng. 110, 270–280.
Roberts, A., Thomas, B., Sewell, P., Khan, Z., Balmain, S., Gillman, J., 2016. Current tidal power technologies and their suitability for applications in coastal and marine areas. J. Ocean Eng. Mar. Energy 2 (2), 227–245.
Sahim, K., Ihtisan, K., Santoso, D., Sipahutar, R., 2014. Experimental study of darrieus-savonius water turbine with deflector: effect of deflector on the performance. Int. J. Rotating Mach. 2014.
Salleh, M.B., Kamaruddin, N.M., Mohamed-Kassim, Z., 2020. The effects of deflector longitudinal position and height on the power performance of a conventional Savonius turbine. Energy Convers. Manag. 226 (August), 113584.
Vermaak, H.J., Kusakana, K., Koko, S.P., 2014. Status of Micro-hydrokinetic River Technology in Rural Applications: A Review of Literature. Renewable and Sustainable Energy Reviews.